# Plasmonic Organic Solar Cells Employing Nanobump Assembly *via* Aerosol-Derived Nanoparticles

**Kinam Jung,[†,§,⊥] Hyung-Jun Song,[‡,§,⊥] Gunhee Lee,[†,§] Youngjun Ko,[‡,§] KwangJun Ahn,[§] Hoseop Choi,[†,§] Jun Young Kim,[‡,§] Kyungyeon Ha,[†,§] Jiyun Song,[‡,§] Jong-Kwon Lee,[§,*] Changhee Lee,[‡,§,*] and Mansoo Choi[†,§,*]**

[†]Division of WCU Multiscale Mechanical Design, School of Mechanical and Aerospace Engineering, Seoul National University, Seoul 151-742, Republic of Korea, [‡]Department of Electrical and Computer Engineering, Seoul National University, Seoul 151-742, Republic of Korea, and [§]Global Frontier Center for Multiscale Energy Systems, Seoul National University, Seoul 151-744, Republic of Korea. [⊥]These authors contributed equally to this work.

**ABSTRACT** We report the effect of a nanobump assembly (NBA) constructed with molybdenum oxide ($MoO_3$) covering Ag nanoparticles (NPs) under the active layer on the efficiency of plasmonic polymer solar cells. Here, the NPs with precisely controlled concentration and size have been generated by an atmospheric evaporation/condensation method and a differential mobility classification and then deposited on an indium tin oxide electrode *via* room temperature aerosol method. NBA structure is made by enclosing NPs with $MoO_3$ layer *via* vacuum thermal evaporation to isolate the undulated active layer formed onto the underlying protruded NBA. Simulated scattering cross sections of the NBA structure reveal higher intensities with a strong forward scattering effect than those from the flat buffer cases. Experimental results of the device containing the NBA show 24% enhancement in short-circuit current density and 18% in power conversion efficiency compared to the device with the flat $MoO_3$ without the NPs. The observed improvements are attributed to the enhanced light scattering and multireflection effects arising from the NBA structure combined with the undulated active layer in the visible and near-infrared regions. Moreover, we demonstrate that the NBA adopted devices show better performance with longer exciton lifetime and higher light absorption in comparison with the devices with Ag NPs incorporated flat poly(3,4-ethylenedioxythiophene):poly(styrenesulfonate) (PEDOT:PSS). Thus, the suggested approach provides a reliable and efficient light harvesting in a broad range of wavelength, which consequently enhances the performance of various organic solar cells.

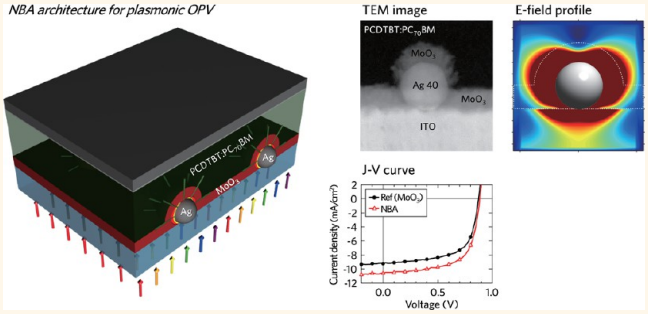


**KEYWORDS:** organic solar cell · nanobump assembly · plasmonic effect · multireflection · nanoparticles · aerosol process

Bulk heterojunction organic photovoltaics (OPVs) consisting of an interpenetrating donor–acceptor network have been extensively studied for their advantages such as thinness, light weight, flexibility, large-area features, as well as simple and cost-effective processes.[1,2] It is well-known that the thickness of OPVs is limited to several tens of nanometers for the effective charge collection with reduced recombination losses due to lower mobility and shorter exciton diffusion length of organic materials compared to inorganic ones.[2,3] However, such thin film structure leads to insufficient light absorption in a photoactive layer, so the efficient light trapping and coupling with the active layer are required to improve the device efficiency. In this respect, metal nanoparticles (NPs) or nanostructures incorporated in single and tandem OPVs have been reported to improve efficiency in device performance,[4−10] which is mainly attributed to plasmonic near-field enhancement and prolonged optical paths of the incident light onto the active layer by scattering elements.[9,11,12]

Meanwhile, the placement of metal NPs at different locations of OPVs enables one to manipulate different mechanisms for optical and (or) electrical enhancement in power conversion efficiency (PCE).[7,12,13] When a polymer based active layer and metal NPs are combined, the PCE is enhanced by the improvement in light absorption or

* Address correspondence to mchoi@snu.ac.kr, chlee7@snu.ac.kr, jklee7@snu.ac.kr.

Received for review December 4, 2013 and accepted February 17, 2014.

**Published online February 17, 2014**
**10.1021/nn500276n**

electrical conductivity, but there is a concern on the possibility of exciton quenching in the active layer.[14,15] Thus, metal NPs are mainly incorporated in the interlayer of conventional OPVs between the indium tin oxide (ITO) anode and the active layer, poly(3,4-ethylenedioxythiophene):poly(styrenesulfonate) (PEDOT:PSS), and there have been reports demonstrating the enhancement in the short-circuit current ($J_{SC}$) and the open-circuit voltage ($V_{OC}$).[5,16,17] In those cases, the metallic NPs such as Ag, Au, and Cu have been mostly embedded within the PEDOT:PSS *via* wet chemical synthesis.[5,18] However, this wet approach involves large amounts of solvents and needs to use surfactants to avoid aggregation among the NPs. Also, there exist contamination problems from impurities during the particle generation, and it is hard to control the concentration and distribution of the NPs during a spin coating process. Moreover, the PEDOT:PSS layer has acidic and hygroscopic features, leading to instability of a device which also arises from etching the ITO electrode and migrating indium to an active layer.[19] Furthermore, degraded PEDOT:PSS is considered as a part of an insulating layer that would deteriorate the device performance.[20] In this regard, several metal oxides such as molybdenum oxide ($MoO_3$), vanadium oxide, tungsten oxide, and nickel oxide have been demonstrated as efficient hole extraction materials for OPV devices to replace the PEDOT:PSS.[21−23] Especially, $MoO_3$ is more stable in the air compared to the PEDOT:PSS and prevents the diffusion of moisture or oxygen into the active layer, resulting in longer lifetime or lower degradation rate.[19] Hence, the OPVs fabricated with this oxide buffer layer have better performance in current density, mobility, and charge carrier conduction with good stability than the devices with the PEDOT:PSS layer.[19,24] Additionally, thermally evaporated metal oxide layer can uniformly follow the surface morphology of underlying nanostructures, while the PEDOT:PSS layer tends to maintain its flat morphology even on textured structures.

In recent studies, $MoO_3$/Ag NPs/$MoO_3$ structure[25,26] and solution-processed Ag NPs-$MoO_3$ composite film[27] as a hole extraction layer (HEL) have been located on the flat active layer for inverted-type organic solar cells to enhance device performance by the enhanced light absorption *via* plasmonic backscattering[25,26] and the improvement of the carrier transport,[27] respectively. Here, the NPs were floated randomly inside the $MoO_3$ layer, while the active layer formed a flat shape. To fully use the conformal property of the $MoO_3$ and, as a consequence, to induce enhanced light-matter interaction in the active layer, the NPs could be deposited prior to the active layer. In such case, the $MoO_3$ covering the NPs, deposited on an ITO electrode, as a HEL has a bumped shape, and the active layer itself is forced to have an undulated structure by the underlying $MoO_3$/Ag NPs. The increased interface area between the active layer and the anode electrode can be expected to contribute to the PCE enhancement in optical as well as electrical aspects.[28] In spite of these advantages, there have been few reports on the NPs embedded nanobump-plasmonic architecture placed under the active layer to enhance the PCE of OPVs, due to the inherent difficulty to precisely form textured metal-structures by conventional wet chemical process. To generate metallic NPs and nanostructures in a controlled manner, an aerosol approach utilizing the evaporation and condensation methods has been extensively studied since the work of Scheibel and Porstendörfer,[29] demonstrating various shapes and sizes of generated NPs[30] and local heating control.[31]

Therefore, in this report, we first demonstrate the 18% PCE enhancement of OPVs by implementing the nanobump assembly (NBA), constructed with the protruded $MoO_3$ covering the aerosol-derived Ag NPs, under the active layer in comparison with the device employing the flat HEL with the Ag NPs. Then, the underlying mechanism of enhanced device performance arising from the NBA combined with the undulated active layer is analyzed by simulations of cross sections and absorption spectra, photoluminescence (PL), current density−voltage ($J-V$) characteristics, and incident photon conversion efficiency (IPCE). Moreover, the effect of Ag NP's size and concentration on device performance in the NBA structure is systematically studied in terms of the enhanced light trapping and multireflections through the aforementioned theoretical and experimental works.

## RESULTS AND DISCUSSION

Figure 1a−e show the fabrication process for the plasmonic OPVs employing the NBA structure. First, we prepared an ITO-coated glass substrate, and then Ag NPs synthesized and classified by atmospheric evaporation/condensation and differential mobility classification methods were deposited on the ITO by room temperature aerosol process. After covering these Ag NPs with 20 nm vacuum-thermally evaporated $MoO_3$ to implement the NBA, the mixture of the poly[*N*-9″-hepta-decanyl-2,7-carbazole-alt-5,5-(4′,7′-di-2-thienyl-2′,1′,3′-benzothiadiazole) (PCDTBT)/[6,6]-phenyl $C_{70}$ butyric acid methyl-ester ($PC_{70}BM$) was spin-coated on top of the NBA. Finally, the device fabrication was completed by depositing 0.5 nm lithium-fluoride (LiF) and 100 nm aluminum electrode. Figure 1f shows a cross-sectional schematic of the completed OPVs incorporating the NBA structure.

Cross-sectional transmission electron microscopy (TEM) images of the device embedding 40 nm Ag NPs (the left side of Figure 1g) show the conformal $MoO_3$ layer with a thickness of 20 nm on the upper half surface of the NPs, which is thick enough to fully cover the Ag NPs without significantly changing the PCE of devices.[32] In addition, mapping images for each

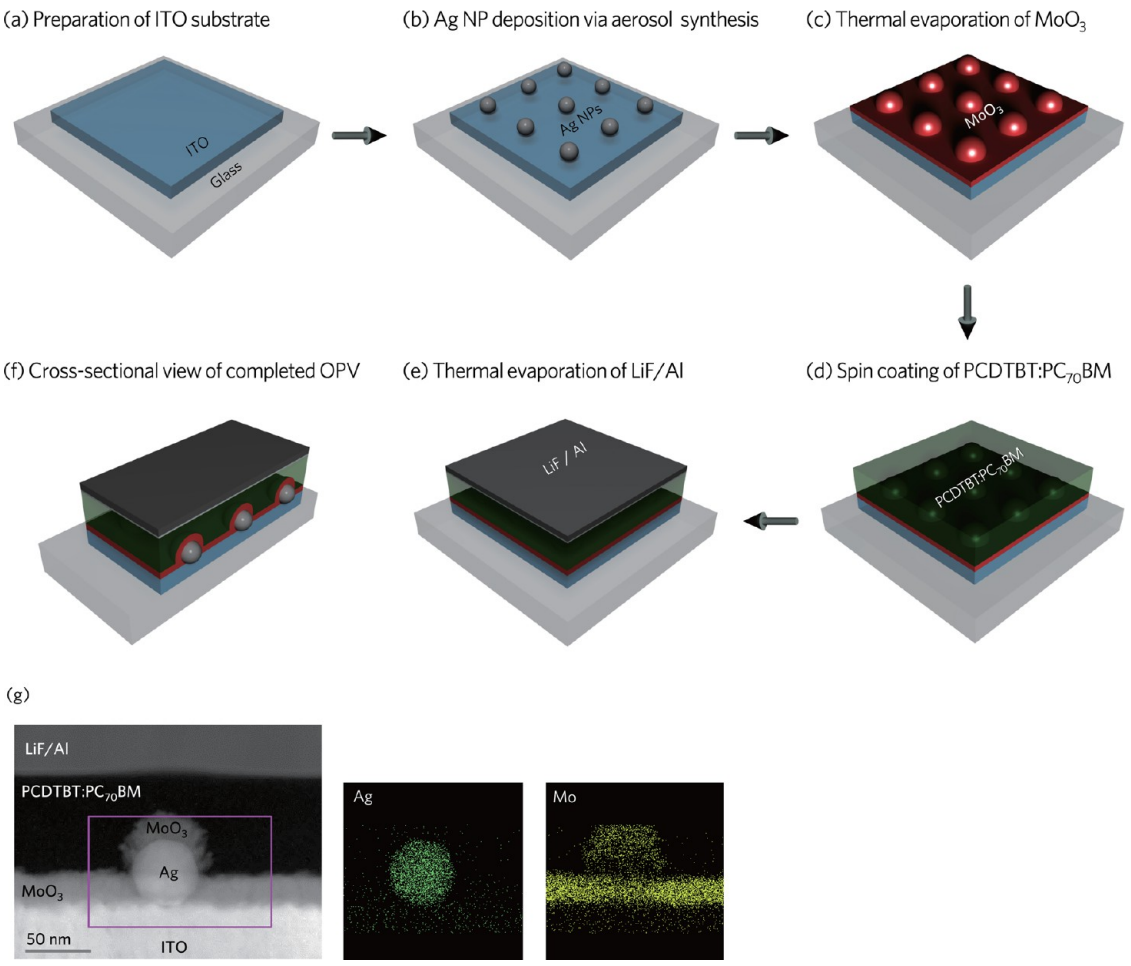


**Figure 1. The fabrication process of the plasmonic OPV employing nanobump assembly: (a) preparation of a cleaned ITO substrate; (b) Ag NPs deposition on the ITO substrate *via* the evaporation and condensation method; (c) thermal evaporation of $MoO_3$ nanobump layer on Ag NPs/ITO; (d) spin coating of PCDTBT:$PC_{70}BM$ active layer on $MoO_3$ layer; (e) thermal evaporation of LiF and Al electrode on the active layer; (f) schematic cross section of completed device, ITO/Ag 40/$MoO_3$/PCDTBT:$PC_{70}BM$/LiF/Al; (g) cross-sectional TEM image and its corresponding EDS data showing the elements of Ag and Mo in the NBA (scale bar: 50 nm).**

material obtained by energy dispersive spectrometer (EDS) analysis in Figure 1g clearly identify the distribution of the $MoO_3$ and the Ag NPs on the ITO electrode, confirming successful formation of the NBA structure with a protruding shape and a textured active layer. In this report, we denote the Ag NPs with an average diameter *d* nm as Ag *d*. Figure S1 also presents the conformal surface morphologies of the NBAs formed on top of Ag 20, 40, and 60. Small-sized Ag 20 and 40 were fully encapsulated by the $MoO_3$, while the lower part of Ag 60 was barely covered with the $MoO_3$ due to the inherent feature of a thermal evaporation process. It is likely that there would be little exciton quenching problem even for Ag 60 enclosed by the $MoO_3$ because the exciton lifetime of polymer casted on it, measured by time-resolved PL, turns out to be the same as those of the NBAs with Ag 20 and 40 (see Figure S2). Therefore, we have successfully fabricated the OPVs that implement the NBA including Ag NPs generated by the evaporation and condensation method.

Figure 2a depicts the experimental setup for the evaporation and condensation method *via* the aerosol process, which consists of a tube furnace, a nano-differential mobility analyzer (nano-DMA), a DMA controller, a neutralizer, a high voltage power supply, two mass flow controllers (MFCs), and a deposition chamber in a glovebox. To deposit Ag NPs on the substrate, a solid silver strip (Alfaesar) was placed at the end of quartz tube located inside the center of the tube furnace (Okdu SiC tube furnace). Two MFCs (Tylan FC280S) were utilized to supply 99.999% $N_2$ carrier gas with 1.5 standard liter per minute into the quartz tube. As the tube furnace was heated at 1150 °C, the Ag NPs were generated. After the high temperature NPs passed through cooling water line maintaining 26 °C, charged NPs were grown by condensation and coagulation processes.[30] The ionized polydispersive Ag NPs were produced *via* a neutralizer (HCT Aerosol Neutralizer 4530), and positively charged monodispersive NPs were classified by the nano-DMA (TSI 308500) and the DMA controller (AERIS). By varying the applied voltage

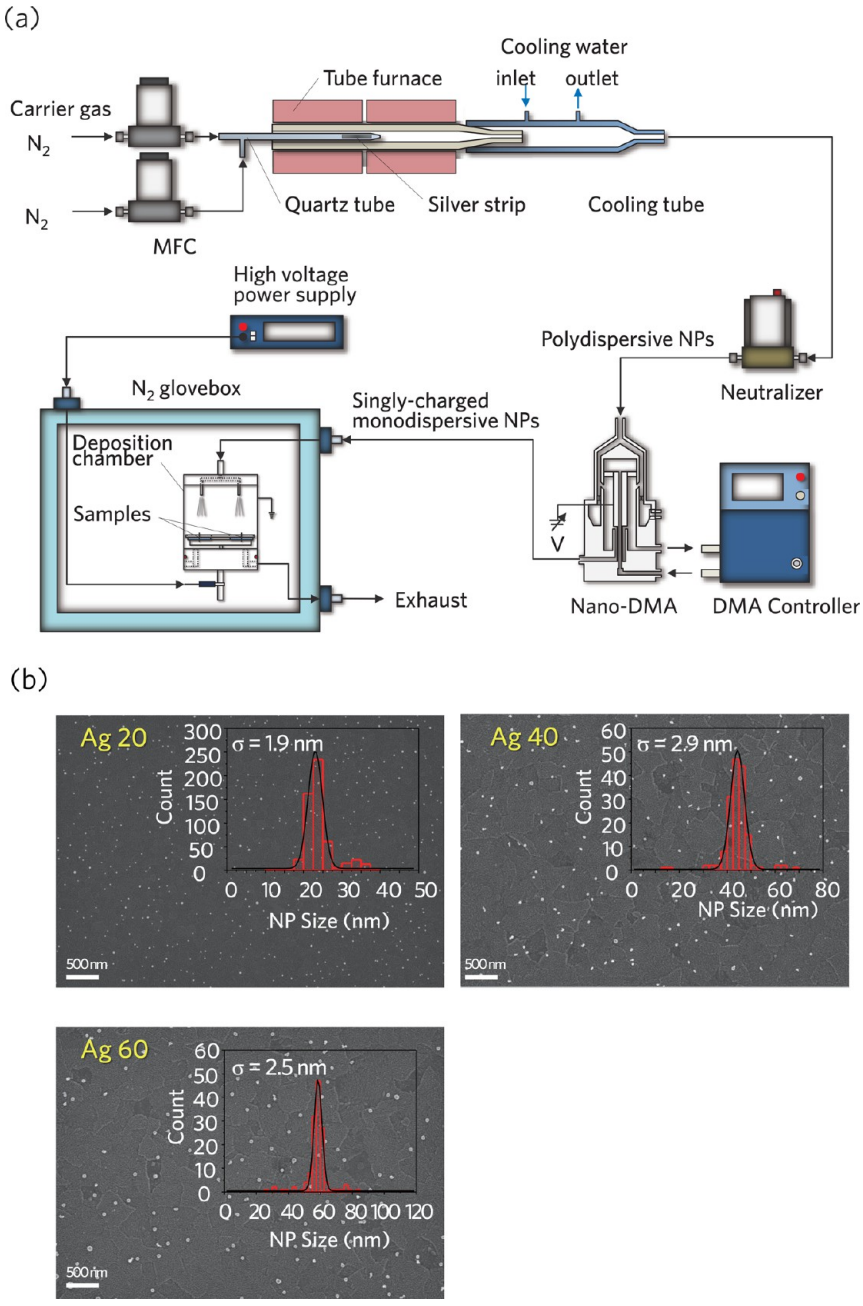


**Figure 2. (a) Schematic of the evaporation and condensation setup to generate Ag NPs and deposit them onto the substrate sample. (b) FE-SEM images of Ag 20, 40, and 60 coated on ITO electrodes. The insets represent the size distribution of the NPs generated by the aerosol method (scale bar: 500 nm).**

according to particle's electrical mobility through the DMA controller such as 1.03, 3.93, and 8.42 kV, we could classify Ag 20, 40, and 60 with well-defined sizes. Here, we set the concentration of charged particle as $3.0 \times 10^5$ $cm^{-3}$ on average, while depositing Ag NPs onto an ITO substrate. By regulating the deposition time, it is possible to control the surface density of Ag NPs on the ITO ranging from 0.2 to $1.5 \times 10^9$ $cm^{-2}$. From the field emission-scanning electron microscopy (FE-SEM) images (×50 000 in magnification, 6.0 $\mu$m × 4.2 $\mu$m in analysis area) in Figure 2b, it is confirmed that incorporated Ag 20, 40, and 60 are uniformly but randomly deposited onto the ITO with small standard deviations of their sizes ($\sigma$): $\sigma$ = 1.9, 2.9, and 2.5 nm for Ag 20, 40, and 60, respectively. This analysis was performed by the ImageJ software (version 1.46r).

To investigate the effect of the NBA structure on the optical enhancement, we analyzed near-field profiles and radiation patterns using a three-dimensional finite-difference time-domain (FDTD) solution package (version 8.4.3, Lumerical solutions) for the Ag 20, 40, and 60 cases in which the NPs deposited on the ITO were enclosed by different HELs ($MoO_3$, PEDOT:PSS) and then encompassed by the same background

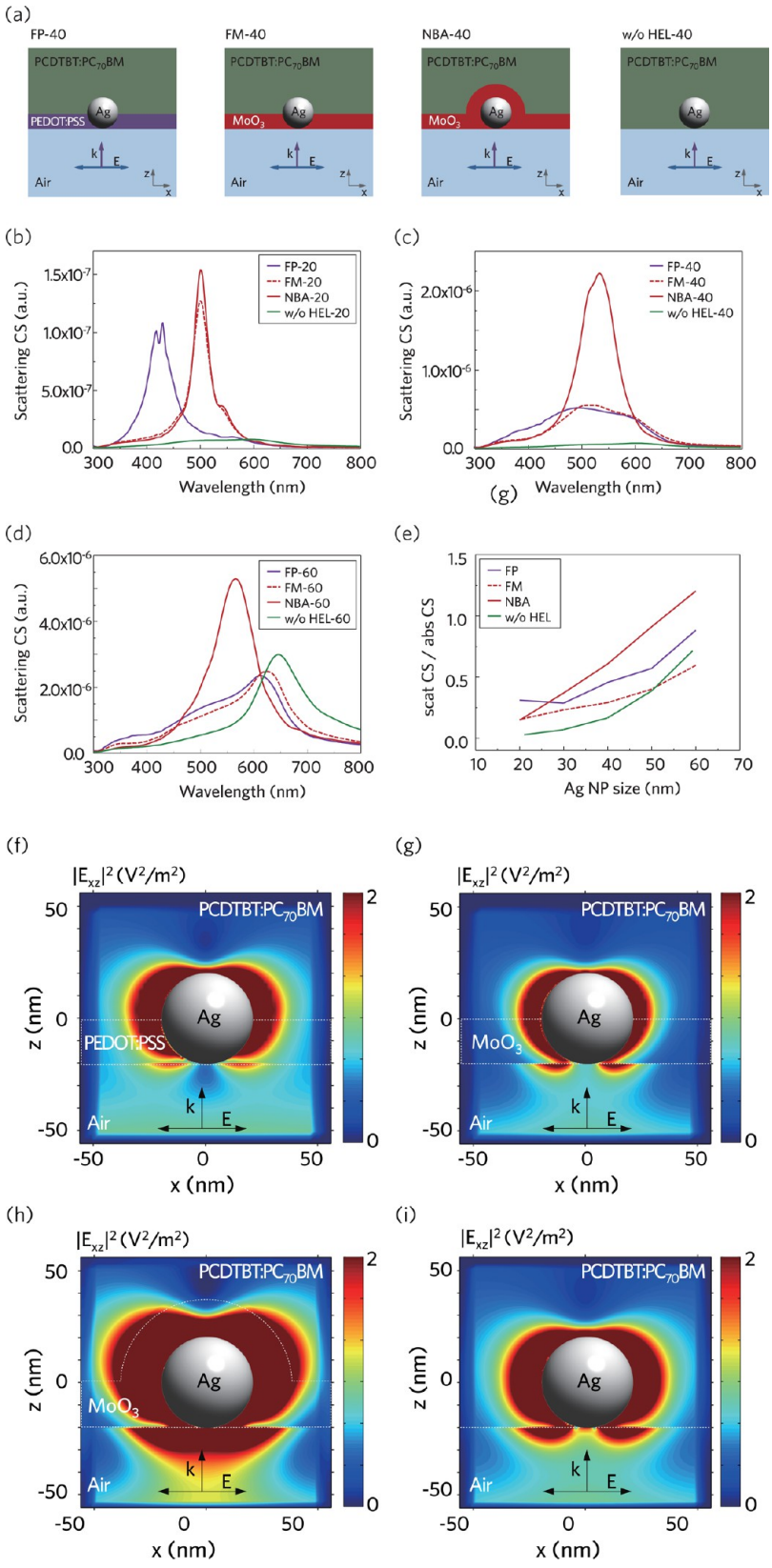


**Figure 3.** (a) Schematics of the FDTD simulation structures of Ag NPs in the different HELs (PEDOT:PSS, flat $MoO_3$, NBA, and without HEL) surrounded by PCDTBT:$PC_{70}$BM, and calculated scattering cross sections (CS) for differently sized Ag NPs: (b) Ag 20, (c) 40, and (d) 60. (e) The ratio of scattering CS to absorption CS as a function of particle diameter in different surrounding media. Here, PF-*d*, FM-*d*, and NBA-*d* represent *d* nm Ag NPs embedded within PEDOT:PSS, flat $MoO_3$, and NBA, respectively, surrounded by PCDTBT:$PC_{70}$BM, while w/o HEL-*d* denotes *d* nm Ag NPs surrounded only by the PCDTBT:$PC_{70}$BM without HEL. Calculated electric field distributions in *xz*-plane at LSPR peak of the NBA-40 ($\lambda$ = 533 nm) for the schematics shown in (a): (f) FP-40, (g) FM-40, (h) NBA-40, and (i) w/o HEL-40.

material (PCDTBT:$PC_{70}BM$). Figure 3a shows the schematics of simulated structures for the d nm Ag NPs embedded in the flat PEDOT:PSS (FP-*d*), flat $MoO_3$ (FM-*d*), and NBA (NBA-*d*) surrounded by the PCDTBT:$PC_{70}BM$, as well as Ag NPs without HEL (w/o HEL-*d*) immersed in the active layer. To compare with the aforementioned cases, Ag NPs within air background case (not shown here) were also simulated. Then, we calculated scattering cross sections (CS) for the Ag 20, 40, and 60 cases where the NPs were located in the four different structures to investigate the variation of scattering intensities with respect to different refractive index (*n*) as shown in Figure 3b–d and Table 1.

Simulated results show that the scattering CS increases and localized surface plasmon resonance (LSPR) peaks are red-shifted when the Ag NP size increases from 20 to 60 nm. The LSPR peak is shifted from 358 to 368 nm as the size of Ag NPs within air background increase from 20 to 60 nm, which is less than those for the other four cases. Since the optical refractive index of the PEDOT:PSS, $MoO_3$, and PCDTBT:$PC_{70}BM$ layers at visible wavelength is larger than that of air ($n = 1$), we anticipate that the LSPR spectra for those structures are more red-shifted compared to that of the NPs within air as the size of NPs increases. Especially, the NBA shows the highest value of scattering CS in the spectral range of 450–600 nm, which is well matched with the main absorption band of the PCDTBT:$PC_{70}BM$. As the diameter of Ag NPs increases from 20 to 60 nm, the degree of spectral shift in LSPR peaks for the NBA is relatively lower than those of the other cases shown in Figure 3b–d, but its intensity level is much higher than the other cases covering the whole absorption band of the active layer.

**TABLE 1. Ratios of Scattering CS to Absorption CS for Differently Sized Ag NPs in Each HEL**

| | NP size (nm) | | | | |
|---|---|---|---|---|---|
| HEL | 20 | 30 | 40 | 50 | 60 |
| FP | 0.31 | 0.29 | 0.46 | 0.57 | 0.88 |
| FM | 0.15 | 0.23 | 0.29 | 0.40 | 0.60 |
| NBA | 0.15 | 0.37 | 0.61 | 0.91 | 1.20 |
| w/o HEL | 0.02 | 0.07 | 0.17 | 0.39 | 0.74 |

Figure 3e represents the ratio of scattering CS to absorption CS for Ag NPs at each maximum value with increasing the diameter from 20 to 60 nm in the four different surrounding materials, illustrating that the ratio is proportional to the Ag NP size. The CS ratio for the NBA-30, 40, 50, and 60 is 0.37, 0.61, 0.91, and 1.20, respectively, higher values than those of the other architectures (see Table 1). Since light scattering is much more dominant factor than absorption loss for extending the optical path length and light trapping efficiency within the active layer, the NBA enclosing Ag NPs within OPVs has a prominent enhancement of the plasmonic effect. To observe the degree of light propagation into the active layers, the electric field profiles for the Ag 40 embedded in different

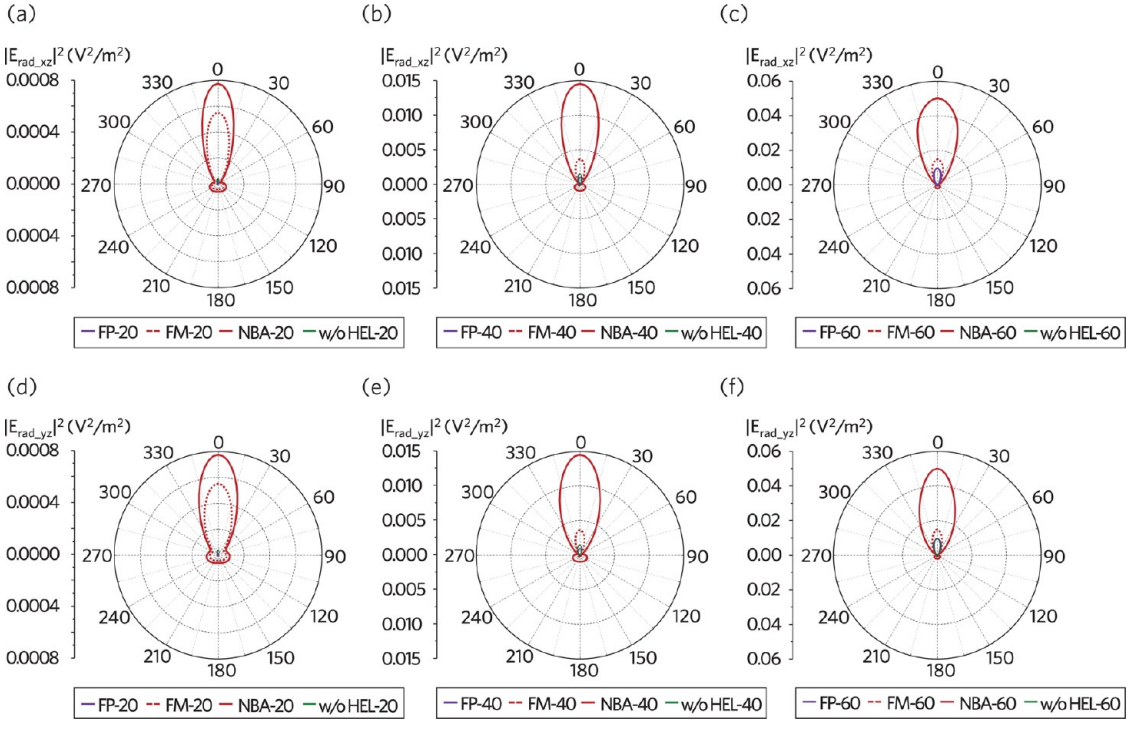


**Figure 4. FDTD simulations on near-field radiation patterns arising from the plasmonic resonance peaks of the NBA for the flat PEDOT:PSS, flat $MoO_3$, NBA, and without HEL embedding (a) Ag 20, (b) 40, and (c) 60 in *xz*-plane, and (d) Ag 20, (e) 40, and (f) 60 in *yz*-plane.**

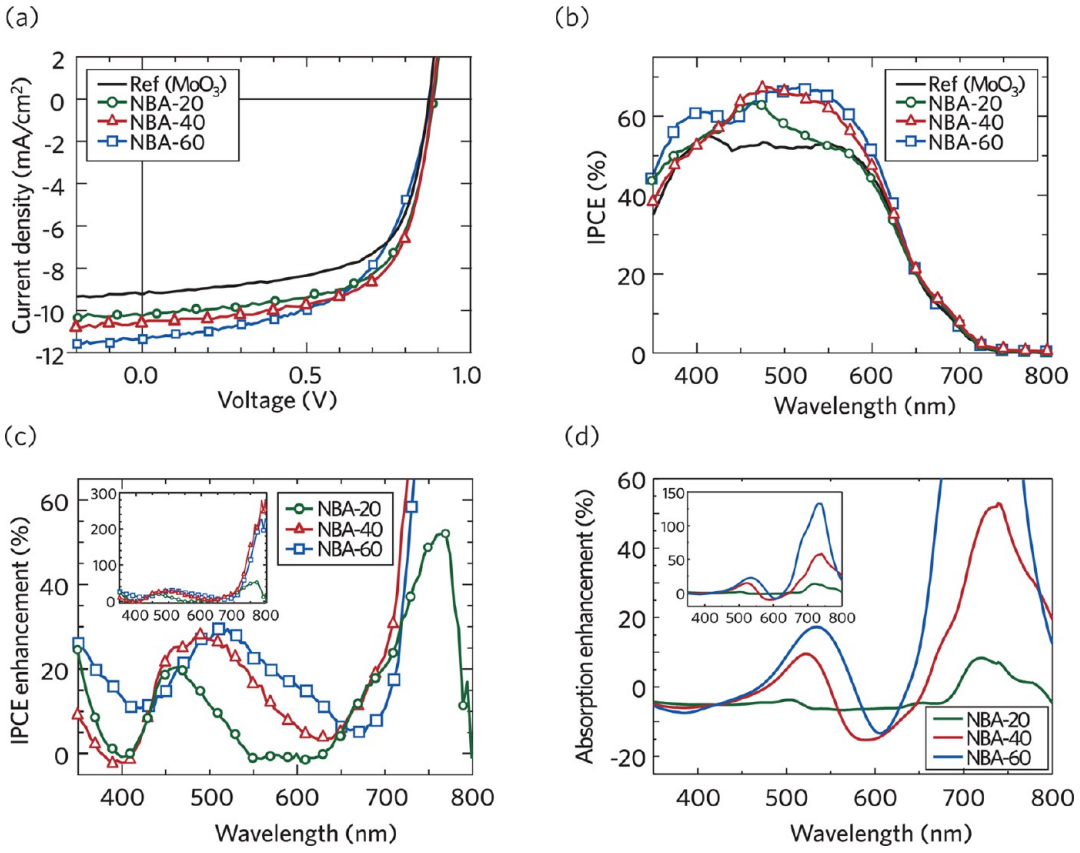


**Figure 5. (a) *J*−*V* characteristics of the plasmonic OPVs with the NBA incorporating differently sized NPs (NBA-20, 40, and 60). (b) IPCEs of the OPVs with the NBA. (c) The IPCE enhancement and (d) calculated absorption enhancement ratios of the plasmonic solar cells as a function of wavelength. The inset graphs in (c) and (d) illustrate the enhancement ratio in a full scale.**

surrounding media were calculated as shown in Figure 3f−i: the scattered light from the NBA propagates farther into the active region than those from the other cases. Thus, the optically amplified fields in the vicinity of Ag NPs *via* LSPR coupling with the incident electromagnetic fields for the NBA case give rise to more enhanced light scattering and trapping effects within the active layer.[12]

Figure 4 shows the calculated near-field radiation patterns of FP-*d*, FM-*d*, NBA-*d*, and w/o HEL-*d*, with respect to *xz*- and *yz*-planes at each plasmon resonance peak of the NBA-20, 40, and 60. In all the cases, the radiated power intensities in *xz*- and *yz*-planes are proportional to the size of Ag NPs. The intensities of near fields for the NBA-20, 40, and 60 within the BHJ layer are higher than those of the other architectures: particularly, the intensities of the NBA both in *xz*- and *yz*-planes are at least four times larger than that of the flat $MoO_3$. Also, the radiated field profiles of all the cases show strong forward scattering characteristics: especially the scattering intensities in *xz*- and *yz*-plane of the NBA are dominant over all the other cases. Thus, the incident light interacting with the NBA can be considerably harvested within the OPVs *via* forward scattering effect. Therefore, the simulation results on the optical near field reveal that the NBA can be a platform for outstandingly enhancing plasmonic OPV compared to the other architectures in the optical point of view.

**TABLE 2. Device Performance of the Plasmonic Solar Cells Containing the NBA with Differently Sized NPs[a]**

| | $J_{SC}$ (mA/cm²) | $V_{OC}$ (V) | FF | efficiency (%) | $R_{SH}$ (kΩ·cm²) |
|---|---|---|---|---|---|
| ref | 9.12 ± 0.10 (9.16) | 0.88 ± 0.01 (0.88) | 0.64 ± 0.01 (0.64) | 5.07 ± 0.08 (5.16) | 2.0 |
| NBA-20 | 10.04 ± 0.09 (10.15) | 0.88 ± 0.01 (0.88) | 0.64 ± 0.01 (0.65) | 5.62 ± 0.15 (5.80) | 2.1 |
| NBA-40 | 10.43 ± 0.12 (10.58) | 0.88 ± 0.01 (0.88) | 0.64 ± 0.01 (0.65) | 5.87 ± 0.17 (6.07) | 2.4 |
| NBA-60 | 11.11 ± 0.24 (11.36) | 0.87 ± 0.01 (0.88) | 0.55 ± 0.02 (0.57) | 5.37 ± 0.26 (5.65) | 0.4 |

[a] The average and standard deviation values of the photovoltaic parameters are shown. The values inside parentheses represent the parameters of OPVs with the highest PCE for each case.

To quantify the effect of the combination of the NBA and the undulated active layer on device performance, OPVs incorporating the NBA with different diameters of 20, 40, and 60 nm were fabricated, and compared with the reference device including 20 nm $MoO_3$ HEL without Ag NPs. The *J*−*V* characteristics of the devices

with the NBA structure and the reference device were taken under AM 1.5G 100 mW/cm$^2$ illumination as shown in Figure 5a. The photovoltaic parameters for each case are summarized in Table 2. The PCE of the devices with NPs is improved from 5.16% in the reference device to 5.80% (NBA-20), 6.07% (NBA-40), and 5.65% (NBA-60), respectively. Interestingly, the observed improvement in the PCE is originated from the increase in $J_{SC}$ from 9.16 mA/cm$^2$ (the reference device) to 10.15 mA/cm$^2$ (NBA-20), 10.58 mA/cm$^2$ (NBA-40), and 11.36 mA/cm$^2$ (NBA-60), accordingly. The enhancement ratio in $J_{SC}$ is more than 10% without changing the $V_{OC}$. Especially, the photocurrent increases as the diameter of incorporated NPs increases, which is coincident with aforementioned optical simulation results showing the enhanced ratio of scattering to absorption CS in the NBA with large-size NPs. To further investigate underlying mechanism for the enhanced $J_{SC}$ from the devices employing the NBA, we have measured exciton generation rates of the devices. The increased exciton generation rate (8.8−23.4%) of the devices with the NBA supports the enhancement in the photocurrent as shown in Figure S3 and Table S1. In addition, it is noted that the absorption intensity of the films with Ag NPs in visible region is higher than that of the counterpart without NPs (see Figure S4), which indicates the match between the enhanced plasmonic peaks induced by the NBA and the absorption band of PCDTBT:$PC_{70}BM$ blend. Also, as the size of NPs increases, the absorption is enhanced, which is consistent with the measured photocurrents. Furthermore, the enhancement in a steady-state PL of PCDTBT layer casted on the NBA at a broad wavelength of 700 - 900 nm (See Figure S2) provides us direct evidence of plasmonic effects.[8,17] Therefore, the higher PCE is mainly attributed to the optical enhancement in the devices embedding the NBA structure.

Despite the highest $J_{SC}$ of the OPV embedding NBA-60, the PCE of it is lower than those of NBA-20 and 40 because of the low fill factor (FF). Since the reverse dark current of the device with NBA-60 is 2 orders of magnitude higher and its shunt resistance is lower compared to those of the others, this reduction of FF can be mainly caused by the increased leakage current and recombination losses[33] (see Figure S5a). The leakage current might be attributed to the thin thickness of the active layer (approximately 20 to 30 nm) in the region where the Ag NPs were inserted between the anode and the cathode (Figure S5d). Many research groups have reported similar drop of FF in devices employing large-size and highly concentrated NPs.[14,15,34] By decreasing the concentration of NPs in NBA-60, the higher PCE of 5.81% was achieved with maintaining FF of 0.65, while the $J_{SC}$ (10.24 mA/cm$^2$) was lowered due to the reduced plasmonic effect by the decreased number of NPs (see Figure S5b and Table S2), which shows good agreement with literatures about the flat interlayers incorporating NPs.[35,36] Consequently, the leakage current arising from the short distance between the cathode and the NBA degrades the device performance in spite of the increased $J_{SC}$. It is not only observed that the PCE of the device containing the NBA-60 with high volume ratio of NPs to the active layer (0.49%) is lowered than that of one with low concentration (0.27%), but device performances of highly concentrated NBA-20 (>0.1%) and 40 (>0.2%) also reduced due to the reduction in $J_{SC}$ as shown in Figure S6. It may be attributed to reduced volume of the active layer arising from the presence of NPs, which augments the leakage current and decreases light harvesting.

To analyze the influence of the NP size on the external quantum efficiency (EQE), the IPCEs of devices with the NBA and the reference device including 20 nm $MoO_3$ HEL without Ag NPs were measured. Figure 5b shows that the IPCE of OPVs with the NBA is higher than that of reference sample, which reflects the enhancement in $J_{SC}$. The effect of the NBA on these OPVs is investigated systematically by comparing measured IPCE with calculated one in terms of enhancement ratio of devices as illustrated in Figure 5c,d. The results show three unique features in the spectral responses of the device. First, the enhancement ratio of measured IPCE increases proportionally to the size of NPs in the spectral range of 400−600 nm, consistent with the optical simulation. The highest IPCE enhancement ratio of each device in this wavelength range increases by 21%, 28%, and 30% in NBA-20, 40, and 60, respectively, with respect to the reference one. The enhancements in experimental IPCE are slightly higher than those of the calculated absorption model because an electrical enhancement coming from an enlarged surface area of the anode with the NBA was not considered in the simulation. Next, the wavelength of the main peak in IPCE enhancement plot (465 nm for NBA-20, 490 nm for NBA-40, and 520 nm for NBA-60) is red-shifted with increasing size of NPs. Simulated absorption data follows the IPCE experimental results regardless of slight difference in the distribution between a calculated model and a fabricated architecture. Even though previous studies have predicted similar phenomenon,[11] to the best of our knowledge, the relationship between the IPCE peak and the NP size enclosed with the metal oxide layer has not been verified experimentally. Our experimental finding of the IPCE peak dependency on the incorporated NP size might have been successfully achieved by the low possibility of aggregation among the NPs and the low deviation of NPs' size in the NBA through the evaporation and condensation method based on the dry aerosol process. Last, the additional enhancement peak at the red and near-infrared (IR) region (650−800 nm) is prominent in both the experimental IPCE and calculated absorption enhancement plots

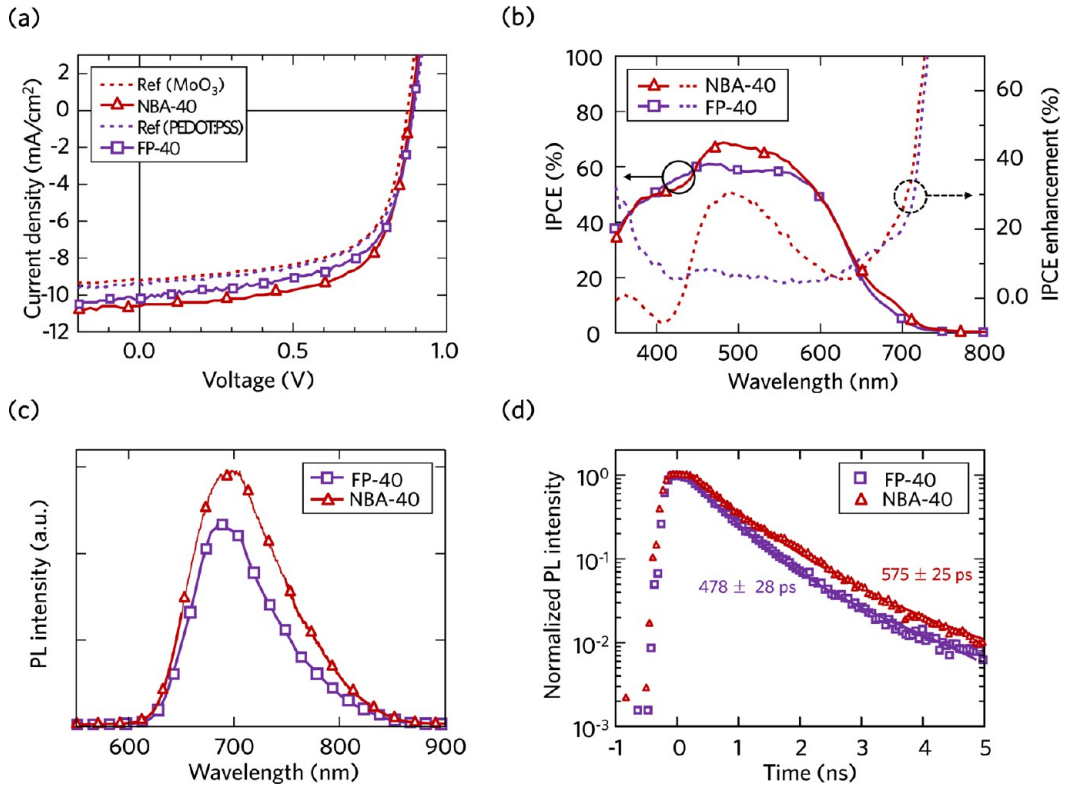


**Figure 6. (a) The *J*−*V* characteristics of devices with different HEL layers. The solid lines denote the devices with Ag 40, while the dash lines represent the devices without Ag NP. (b) The IPCE data and their enhancement ratios compared to each reference sample. (c) Steady-state PL spectra of PCDTBT films with different buffer layers. (d) Time-resolved PL ($\lambda$ = 690 nm) of PCDTBT films with the NBA-40 compared to the FP-40, where the numbers represent the exciton lifetime inside each active material. Here, the measured data (symbols) are fitted using exponential functions (solid lines).**

(the inset of Figure 5c,d), which is not observed in the calculated scattering CS shown in Figure 3. Interestingly, this improvement shown in the range above 650 nm is much higher than that occurring at 450−600 nm. By comparing the absorption of the active layer with and without Al back reflector throughout the simulation, we found that the multireflection between the NBA on the ITO electrode and the Al electrode causes to increase the absorption in low energy light (see Figure S7). But the absorption of the PCDTBT:$PC_{70}BM$ in this region is so low that this enhancement cannot substantially contribute to photocurrent enhancement. If this NBA is applied to near IR absorbing materials, further improvement in device performance is expected.

Furthermore, to identify the difference in the plasmonic effect between the NBA and the conventionally used flat interfacial layers including Ag NPs, devices containing PEDOT:PSS with and without 40 nm of Ag NP were fabricated. The relatively thin PEDOT:PSS (20 nm) was chosen as the HEL for direct comparison with the NBA case.[37] The device structure and all manufacturing procedures except the HEL were exactly the same as those of devices with the NBA. Figure 6a shows the *J*−*V* characteristics of devices with different plasmonic structures. The PCE of the device with FP-40 (5.67%) is improved compared to its counterpart without Ag NPs (5.20%). As the flat PEDOT:PSS is replaced with the NBA structure as a HEL, the PCE of the NBA-40 further increases to 6.07% because of the enhancement in $J_{SC}$ from 10.24 to 10.58 mA/cm$^2$. It should be noted that the device performance of the samples without Ag NPs is very similar to each other regardless of HEL types (Table 3). These results of device performance demonstrate that the NBA structure more significantly influences the photovoltaic characteristic compared to the device with the same sized NPs embedded in the flat PEDOT:PSS.

The enhancement in $J_{SC}$ can be attributed to the higher exciton generation of the device assisted by the NBA because of its excellent optical effects: the LSPR

**TABLE 3. Comparison of Device Performance for the NBA-40 and the FP-40[a]**

| HEL layer | Ag NPs | $J_{SC}$ (mA/cm$^2$) | $V_{OC}$ (V) | FF | efficiency (%) |
|---|---|---|---|---|---|
| NBA | None | 9.12 ± 0.10 (9.16) | 0.88 ± 0.01 (0.88) | 0.64 ± 0.01 (0.64) | 5.07 ± 0.08 (5.16) |
| | NBA-40 | 10.43 ± 0.12 (10.58) | 0.88 ± 0.01 (0.88) | 0.64 ± 0.01 (0.65) | 5.87 ± 0.17 (6.07) |
| Flat PEDOT:PSS | None | 9.18 ± 0.10 (9.19) | 0.89 ± 0.01 (0.89) | 0.62 ± 0.01 (0.63) | 5.08 ± 0.11 (5.20) |
| | FP-40 | 10.10 ± 0.12 (10.24) | 0.89 ± 0.01 (0.89) | 0.61 ± 0.01 (0.62) | 5.57 ± 0.06 (5.63) |

[a] The average and standard deviation values of the photovoltaic parameters are shown. The values inside parentheses represent the parameters of OPVs with the highest PCE for each case.

and near-field analysis. The effects of different optical properties caused by each plasmonic structure on device performance are reflected in the IPCE of two devices as illustrated in Figure 6b. The increase in $J_{SC}$ of the NBA-40 is mainly caused by the increased EQE at the wavelength of 450 − 600 nm, while the IPCE of FP-40 is outstandingly improved at a short wavelength (~350 nm), similar to the previous reports on the devices embedding Ag NPs in PEDOT:PSS layer.[5] This results coincide with the simulated result on the scattering CS (Figure 3c) and the UV−visible light absorption spectra of the PCDTBT:$PC_{70}$BM films casted on the both $MoO_3$ and PEDOT:PSS with Ag NP (see Figure S4). Therefore, it is obvious that the enhanced scattering intensity near the green light with a strong forward direction *via* the combination of the NBA and the undulated active layer makes the photocurrent of device higher compared to the case with flat buffer layers.

In addition, the steady-state PL of the spin-casted PCDTBT films with NBA-40 and FP-40 is supportive evidence to show better optical properties of the NBA. Figure 6c demonstrates that the PL intensity of the NBA-40 is broadly enhanced compared to that of the FP-40. Commonly, the steady-state PL intensity is generally determined by two factors: the resonance frequency overlap between the absorption band gap of polymer and the nanostructure induced plasmonic effects, as well as the decay of photogenerated excitons.[38] The aforementioned simulation and measured results already reveal that the superior optical properties of the NBA contribute to the change of steady-state PL. However, the difference in the steady-state PL between the NBA-40 and FP-40 is bigger than that of $J_{SC}$ for each corresponding device. To distinguish the optical and electrical effect of different plasmonic buffer layers, transient PLs of both films were measured at the wavelength of 690 nm (Figure 6d) and decay times of films on each buffer were estimated by using exponential function.[17] In the films with FP-40, the short exciton lifetime (478 ± 28 ps) is observed, whereas the lifetime of NBA-40 (575 ± 25 ps) is similar to that of film without NPs (see Figure S2b). Generally, the fast decay of exciton is related to high recombination losses and exciton quenching.[17,26] Moreover, it is well-known that the direct contact between metal NPs and polymer layers can be a source of the exciton quenching.[38,39] As a result, the NBA, which has Ag NPs fully covered by the thermally evaporated $MoO_3$, prevents the device from recombination losses, while the exciton quenching can occur at partially disclosed Ag NPs placed in the flat PEDOT:PSS. Therefore, the NBA not only enhances device performance due to its superior optical properties, but also has low recombination losses arising from isolation of the NPs from the active layer without any degradation of the enhanced optical properties. Consequently, it is apparent that the NBA induced plasmonic effect and light scattering are higher than those from the conventional structure.

## CONCLUSIONS

We have demonstrated a considerable enhancement both in $J_{SC}$ and PCE of the plasmonic PCDTBT:$PC_{70}$BM solar cells employing the NBA composed of $MoO_3$ layer and Ag NPs under the active layer, compared to the reference devices including $MoO_3$ HEL without NPs. Here, the NPs with different diameters (Ag 20, 40, and 60) have been generated by the evaporation and condensation method using the aerosol process in dry environment without aggregation, impurity, and contamination issues that can usually happen in the wet synthesis. FDTD calculation results on scattering cross sections and near-field profiles inside the active materials show higher intensities with a strong forward scattering effect in the devices with the NBA than those with the flat PEDOT:PSS. *J*−*V* characteristics show that $J_{SC}$ increases continuously as the size of NPs increases and the best performance is achieved at the device embedding NBA-40. The improved performance depending on the size of NPs is explained by the strong forward light scattering effect coming from near-field enhancement in the vicinity of Ag NP in the visible region, as well as the multireflection between the cathode and the nanobumped anode in the near-IR region. Furthermore, we have presented that the OPVs containing the NBA show better performance than those with PEDOT:PSS incorporating NPs due to smaller recombination losses and higher absorption intensity. Therefore, our approach can be a promising platform for efficient light harnessing in a broad spectral range for use in diverse OPV devices.

## EXPERIMENTAL AND COMPUTATIONAL SECTION

**3D FDTD Simulation for CS and IPCE Enhancement.** We set the incident light source (300−800 nm in wavelength) propagating in *z*-direction with TE polarization (or horizontal polarization), and used symmetric boundary conditions for *x*-, *y*-axes and perfectly matched layer (PML) condition for *z*-axis. We selected total field scatter field (TFSF) light source to the FDTD model. The absorption CS and the scattering CS were calculated by a total field (incident field + scattered field) power monitor and a scattered field power monitor. With the use of these power monitors, power flows induced by the interaction of the incident wave and a particle scatterer were estimated.

Dispersive complex refractive indices (*n*, *k*) for PEDOT:PSS, $MoO_3$, and PCDTBT:$PC_{70}$BM measured by spectroscopic ellipsometer (M2000D,Woollam) were adopted in to the simulation model. It was assumed that both Ag NPs and the NBA were concentric spheres and Ag NPs were point-contacted onto the ITO-coated glass. Also, the ITO and Al electrodes were excluded so as to consider only the scattering effect by plasmonic NPs neglecting

multireflection phenomena between the two electrodes. We also imposed an average interdistance of 200 nm on Ag 20, 40, and 60 from the particle analysis of the SEM images. The thickness for the PEDOT:PSS and $MoO_3$ layers on the ITO-coated glass substrate was fixed at 20 nm to reproduce real device structure.

Finally, the calculated absorption enhancement is compared with the experimental IPCE enhancement. The actual structure of plasmonic OPV was modeled by considering the measured thickness of the device with and without NPs. The plane wave source under AM 1.5G illumination was imposed on the model and the rest of boundary conditions were the same as the near field CS simulations. With the insertion of power monitor into the model, the absorption enhancement within plasmonic architecture was extracted.

**Device Fabrication and Electro-Optical Measurement.** The devices were fabricated on ITO-coated glass substrates with a sheet resistance of 20 $\Omega/cm^2$. The ITO patterned substrates were precleaned with acetone for 15 min and isopropyl alcohol for 15 min and were dried in a vacuum oven. And then, the ITO-coated glasses were treated with UV-ozone. The various sizes of silver NPs were deposited on the ITO using the evaporation and condensation method in the nitrogen glovebox. Afterward, the mixture of the PCDTBT:$PC_{70}BM$ in dichlorobenzene (1:4 weight ratio, 20 mg/mL) was spin-casted at 600 rpm for 60 s on top of the $MoO_3$ layer of 20 nm thickness by thermal evaporation process to construct nanobump arrays and was annealed at a high vacuum ($<10^{-6}$ Torr) chamber for 2 h. The active layer was 80−90 nm in thickness. Finally, the device fabrication was completed by thermal evaporation of 0.5 nm LiF for electron extraction layer and 100 nm Al as the cathode through shadow masks under high vacuum chamber. For comparison, the reference device without Ag NPs was also fabricated. In addition, the films without LiF and the cathode electrode for UV−visible absorption spectra and the ones substituting the active layer with 80 nm PCDTBT for PL measurement were fabricated as well.

The *J*−*V* characteristics were measured using a Keithley 237 source measurement unit under AM 1.5G illumination condition at an intensity of 100 $mW/cm^2$ with an Oriel S013A solar simulator. IPCE spectra of devices were obtained using Oriel IQE 200 model, which combined monochromator and lock-in amplifier by comparison to a calibrated silicon photodiode. The *J*−*V* feature and IPCE measurement procedures were performed in the nitrogen glovebox to prevent the device degradations. For UV−visible spectroscopy measurement, the Cary 5000 UV−vis-NIR spectrophotometer (Agilent Technologies) with integrating sphere system was used. On the other hand, the steady-state and time-resolved PL excited by 405 nm laser diode were recorded using iHR320 (Horiba, Ltd.).

*Conflict of Interest:* The authors declare no competing financial interest.

*Acknowledgment.* This work was supported by the Global Frontier R&D Program on Center for Multiscale Energy System funded by the National Research Foundation under the Ministry of Science, ICT & Future, Korea (2011-0031561, 2011-0031567, and 2012M3A6A7054855).

*Supporting Information Available:* TEM images of nanobump assembly, PL data of PCDTBT layer with the different HELs including different sizes of NPs, UV−visible absorption, exciton generation rate of devices, the dependence of the NP concentration on device performance, and the calculated absorption spectra of the device with and without cathode layer. This material is available free of charge *via* the Internet at http://pubs.acs.org.

## REFERENCES AND NOTES

1. Yu, G.; Gao, J.; Hummelen, J. C.; Wudl, F.; Heeger, A. J. Polymer Photovoltaic Cells: Enhanced Efficiencies *via* a Network of Internal Donor-Acceptor Heterojunctions. *Science* **1995**, *270*, 1789–1791.
2. Li, G.; Zhu, R.; Yang, Y. Polymer Solar Cells. *Nat. Photonics* **2012**, *6*, 153–161.
3. Terao, Y.; Sasabe, H.; Adachi, C. Correlation of Hole Mobility, Exciton Diffusion Length, and Solar Cell Characteristics in Phthalocyanine/Fullerene Organic Solar Cells. *Appl. Phys. Lett.* **2007**, *90*, 103515.
4. Gan, Q.; Bartoli, F. J.; Kafafi, Z. H. Plasmonic-Enhanced Organic Photovoltaics: Breaking the 10% Efficiency Barrier. *Adv. Mater.* **2013**, *25*, 2385–2396.
5. Lu, L.; Luo, Z.; Xu, T.; Yu, L. Cooperative Plasmonic Effect of Ag and Au Nanoparticles on Enhancing Performance of Polymer Solar Cells. *Nano Lett.* **2013**, *13*, 59–64.
6. Yang, J.; You, J.; Chen, C.-C.; Hsu, W.-C.; Tan, H.; Zhang, X. W.; Hong, Z.; Yang, Y. Plasmonic Polymer Tandem Solar Cell. *ACS Nano* **2011**, *5*, 6210–6217.
7. Wang, D. H.; Kim, D. Y.; Choi, K. W.; Seo, J. H.; Im, S. H.; Park, J. H.; Park, O. O.; Heeger, A. J. Enhancement of Donor−Acceptor Polymer Bulk Heterojunction Solar Cell Power Conversion Efficiencies by Addition of Au Nanoparticles. *Angew. Chem., Int. Ed.* **2011**, *50*, 5519–5523.
8. Wu, B.; Oo, T. Z.; Li, X.; Liu, X.; Wu, X.; Yeow, E. K. L.; Fan, H. J.; Mathews, N.; Sum, T. C. Efficiency Enhancement in Bulk-Heterojunction Solar Cells Integrated with Large-Area Ag Nanotriangle Arrays. *J. Phys. Chem. C* **2012**, *116*, 14820–14825.
9. Hsiao, Y.-S.; Charan, S.; Wu, F.-Y.; Chien, F.-C.; Chu, C.-W.; Chen, P.; Chen, F.-C. Improving the Light Trapping Efficiency of Plasmonic Polymer Solar Cells through Photon Management. *J. Phys. Chem. C* **2012**, *116*, 20731–20737.
10. Kao, C.-S.; Chen, F.-C.; Liao, C.-W.; Huang, M. H.; Hsu, C.-S. Plasmonic-Enhanced Performance for Polymer Solar Cells Prepared with Inverted Structures. *Appl. Phys. Lett.* **2012**, *101*, 193902.
11. Yang, X.; Chueh, C.-C.; Li, C.-Z.; Yip, H.-L.; Yin, P.; Chen, H.; Chen, W.-C.; Jen, A. K.-Y. High-Efficiency Polymer Solar Cells Achieved by Doping Plasmonic Metallic Nanoparticles into Dual Charge Selecting Interfacial Layers to Enhance Light Trapping. *Adv. Energy Mater.* **2013**, *3*, 666–673.
12. Atwater, H. A.; Polman, A. Plasmonics for Improved Photovoltaic Devices. *Nat. Mater.* **2010**, *9*, 205–213.
13. Qu, D.; Liu, F.; Huang, Y.; Xie, W.; Xu, Q. Mechanism of Optical Absorption Enhancement in Thin Film Organic Solar Cells with Plasmonic Metal Nanoparticles. *Opt. Express* **2011**, *19*, 24795–24803.
14. Spyropoulos, G. D.; Stylianakis, M. M.; Stratakis, E.; Kymakis, E. Organic Bulk Heterojunction Photovoltaic Devices with Surfactant-Free Au Nanoparticles Embedded in the Active Layer. *Appl. Phys. Lett.* **2012**, *100*, 213904.
15. Xue, M.; Li, L.; Tremolet de Villers, B. J.; Shen, H.; Zhu, J.; Yu, Z.; Stieg, A. Z.; Pei, Q.; Schwartz, B. J.; Wang, K. L. Charge-Carrier Dynamics in Hybrid Plasmonic Organic Solar Cells with Ag Nanoparticles. *Appl. Phys. Lett.* **2011**, *98*, 253302.
16. Kalfagiannis, N.; Karagiannidis, P. G.; Pitsalidis, C.; Panagiotopoulos, N. T.; Gravalidis, C.; Kassavetis, S.; Patsalas, P.; Logothetidis, S. Plasmonic Silver Nanoparticles for Improved Organic Solar Cells. *Sol. Energy Mater. Sol. Cells* **2012**, *104*, 165–174.
17. Wu, J.-L.; Chen, F.-C.; Hsiao, Y.-S.; Chien, F.-C.; Chen, P.; Kuo, C.-H.; Huang, M. H.; Hsu, C.-S. Surface Plasmonic Effects of Metallic Nanoparticles on the Performance of Polymer Bulk Heterojunction Solar Cells. *ACS Nano* **2011**, *5*, 959–967.
18. Ye, J.; Verellen, N.; Van Roy, W.; Lagae, L.; Maes, G.; Borghs, G.; Van Dorpe, P. Plasmonic Modes of Metallic Semishells in a Polymer Film. *ACS Nano* **2010**, *4*, 1457–1464.
19. Sun, Y.; Takacs, C. J.; Cowan, S. R.; Seo, J. H.; Gong, X.; Roy, A.; Heeger, A. J. Efficient, Air-Stable Bulk Heterojunction Polymer Solar Cells Using MoOx as the Anode Interfacial Layer. *Adv. Mater.* **2011**, *23*, 2226–2230.
20. Kawano, K.; Pacios, R.; Poplavskyy, D.; Nelson, J.; Bradley, D. D. C.; Durrant, J. R. Degradation of Organic Solar Cells Due to Air Exposure. *Sol. Energy Mater. Sol. Cells* **2006**, *90*, 3520–3530.
21. Shrotriya, V.; Li, G.; Yao, Y.; Chu, C.-W.; Yang, Y. Transition Metal Oxides as the Buffer Layer for Polymer Photovoltaic Cells. *Appl. Phys. Lett.* **2006**, *88*, 073508.

22. Han, S.; Shin, W. S.; Seo, M.; Gupta, D.; Moon, S.-J.; Yoo, S. Improving Performance of Organic Solar Cells Using Amorphous Tungsten Oxides as an Interfacial Buffer Layer on Transparent Anodes. *Org. Electron.* **2009**, *10*, 791–797.
23. Irwin, M. D.; Buchholz, D. B.; Hains, A. W.; Chang, R. P. H.; Marks, T. J. p-Type Semiconducting Nickel Oxide as an Efficiency-Enhancing Anode Interfacial Layer in Polymer Bulk-Heterojunction Solar Cells. *Proc. Natl. Acad. Sci. U.S.A.* **2008**, *105*, 2783–2787.
24. Kim, D. Y.; Subbiah, J.; Sarasqueta, G.; So, F.; Ding, H.; Irfan; Gao, Y. The Effect of Molybdenum Oxide Interlayer on Organic Photovoltaic Cells. *Appl. Phys. Lett.* **2009**, *95*, 093304.
25. Cheng, P.-P.; Ma, G.-F.; Li, J.; Xiao, Y.; Xu, Z.-Q.; Fan, G.-Q.; Li, Y.-Q.; Lee, S.-T.; Tang, J.-X. Plasmonic Backscattering Enhancement for Inverted Polymer Solar Cells. *J. Mater. Chem.* **2012**, *22*, 22781–22787.
26. Cheng, P.-P.; Zhou, L.; Li, J.-A.; Li, Y.-Q.; Lee, S.-T.; Tang, J.-X. Light Trapping Enhancement of Inverted Polymer Solar Cells with a Nanostructured Scattering Rear Electrode. *Org. Electron.* **2013**, *14*, 2158–2163.
27. Li, X.; Choy, W. C. H.; Xie, F.; Zhang, S.; Hou, J. Room-Temperature Solution-Processed Molybdenum Oxide as a Hole Transport Layer with Ag Nanoparticles for Highly Efficient Inverted Organic Solar Cells. *J. Mater. Chem. A* **2013**, *1*, 6614–6621.
28. Wang, D. H.; Seifter, J.; Park, J. H.; Choi, D.-G.; Heeger, A. J. Efficiency Increase in Flexible Bulk Heterojunction Solar Cells with a Nano-Patterned Indium Zinc Oxide Anode. *Adv. Energy Mater.* **2012**, *2*, 1319–1322.
29. Scheibel, H. G.; Porstendörfer, J. Generation of Monodisperse Ag- and NaCl-Aerosols with Particle Diameters between 2 and 300 nm. *J. Aerosol Sci.* **1983**, *14*, 113–126.
30. Magnusson, M. H.; Deppert, K.; Malm, J.-O.; Bovin, J.-O.; Samuelson, L. Gold Nanoparticles: Production, Reshaping, and Thermal Charging. *J. Nanopart. Res.* **1999**, *1*, 243–251.
31. Jung, J. H.; Oh, H. C.; Noh, H. S.; Ji, J. H.; Kim, S. S. Metal Nanoparticle Generation Using a Small Ceramic Heater with a Local Heating Area. *J. Aerosol Sci.* **2006**, *37*, 1662–1670.
32. Noh, S.; Suman, C. K.; Lee, D.; Kim, S.; Lee, C. Study of Buffer Layer Thickness on Bulk Heterojunction Solar Cell. *J. Nanosci. Nanotechnol.* **2010**, *10*, 6815–6818.
33. Qi, B.; Wang, J. Fill Factor in Organic Solar Cells. *Phys. Chem. Chem. Phys.* **2013**, *15*, 8972–8982.
34. Lee, J. H.; Park, J. H.; Kim, J. S.; Lee, D. Y.; Cho, K. High Efficiency Polymer Solar Cells with Wet Deposited Plasmonic Gold Nanodots. *Org. Electron.* **2009**, *10*, 416–420.
35. Baek, S.-W.; Noh, J.; Lee, C.-H.; Kim, B.; Seo, M.-K.; Lee, J.-Y. Plasmonic Forward Scattering Effect in Organic Solar Cells: A Powerful Optical Engineering Method. *Sci. Rep.* **2013**, *3*, 1726.
36. Dunbar, R. B.; Pfadler, T.; Schmidt-Mende, L. Highly Absorbing Solar Cells—A Survey of Plasmonic Nanostructures. *Opt. Express* **2012**, *20*, A177–A189.
37. Dennler, G.; Scharber, M. C.; Brabec, C. J. Polymer-Fullerene Bulk-Heterojunction Solar Cells. *Adv. Mater.* **2009**, *21*, 1323–1338.
38. Wang, J.; Lee, Y.-J.; Chadha, A. S.; Yi, J.; Jespersen, M. L.; Kelley, J. J.; Nguyen, H. M.; Nimmo, M.; Malko, A. V.; Vaia, R. A.; *et al.* Effect of Plasmonic Au Nanoparticles on Inverted Organic Solar Cell Performance. *J. Phys. Chem. C* **2013**, *117*, 85–91.
39. Salvador, M.; MacLeod, B. A.; Hess, A.; Kulkarni, A. P.; Munechika, K.; Chen, J. I. L.; Ginger, D. S. Electron Accumulation on Metal Nanoparticles in Plasmon-Enhanced Organic Solar Cells. *ACS Nano* **2012**, *6*, 10024–10032.